

# Detecting Cracks in Ceramic Matrix Composites by Electrical Resistance

Craig Smith and Andrew Gyekenyesi  
Ohio Aerospace Institute  
Cleveland, Ohio

## ABSTRACT

The majority of damage in SiC/SiC ceramic matrix composites subjected to monotonic tensile loads is in the form of distributed matrix cracks. These cracks initiate near stress concentrations, such as 90° fiber tows or large matrix pores and continue to accumulate with additional stress until matrix crack saturation is achieved. Such damage is difficult to detect with conventional nondestructive evaluation techniques (immersion ultrasonics, x-ray, etc.). Monitoring a specimen's electrical resistance change provides an indirect approach for monitoring matrix crack density. Sylramic-iBN fiber-reinforced SiC composites with a melt infiltrated (MI) matrix were tensile tested at room temperature. Results showed an increase in resistance of more than 500% prior to fracture, which can be detected either in situ or post-damage. A relationship between resistance change and matrix crack density was also determined.

## KEYWORD LIST

Ceramic matrix composite (CMC), electrical resistance, cracking, nondestructive evaluation, damage

## 1. INTRODUCTION

Structural ceramic matrix composites (CMC) are able to withstand elevated temperatures and extreme environmental conditions (well beyond the limits of metals). These characteristics make them desirable for various high temperature aerospace applications where traditional nickel-based super-alloys are currently utilized. Silicon carbide fiber-reinforced silicon carbide matrix (SiC/SiC) is one particular CMC system that has been identified by NASA for use in high-temperature oxidizing environments<sup>1</sup>. In general, SiC/SiC composites have low density, high thermal conductivity, good toughness (especially when compared to monolithic ceramics), and good oxidation resistance. Some of the potential applications that have been identified include hot-section components of gas turbines<sup>2,3</sup>, aerojet engines<sup>4</sup>, thermal protection systems<sup>5</sup>, and hot-control surfaces<sup>6</sup>. The advantages of using CMCs in these areas include reduced cooling air requirements, lower weight, simpler component design, longer service life, as well as the associated higher thrust capacity regarding turbines<sup>7</sup>.

Much work has been done to characterize the mechanical behavior of SiC/SiC composites under various mechanical load and environmental scenarios. Even so, the danger exists for catastrophic failure during service as a result of the statistical and brittle nature of ceramic constituents, as well as general damage progression in the form of distributed matrix cracks (transverse and longitudinal) and fiber breaks. Early detection of this damage and the associated property changes is essential for structural applications. Accurately detecting the damage (either in situ or by inspecting the component during downtime) will improve vehicle safety by providing a warning to the operator when the material is damaged/compromised beyond a pre-defined safe limit.

Damage in SiC/SiC composites begins with transverse matrix cracks that develop near stress concentrations (e.g., 90° tows or open pores). After initiation, these cracks continue to grow through the thickness with additional stress and/or time<sup>8</sup>. Conventional nondestructive evaluation (NDE) techniques, such as x-ray and immersion ultrasonics, have low sensitivities to such small scale, distributed damage. Overall system noise (due to the complexities of the constituents as well as pre-existing flaws) masks the new damage. In addition, the through-thickness nature of these techniques requires observations to occur parallel to the matrix cracks. Lastly, these methods typically require the component to be removed from service for inspection causing excessive down time.

Electrical resistance monitoring is a method that shows promise toward overcoming many of the deficiencies of the above techniques. In principle, as transverse matrix cracks propagate perpendicular to the loading direction, the current carrying capability in the longitudinal direction diminishes. The resistance can also be monitored in situ; eliminating the need for long downtimes. For these reasons, correlating electrical resistance changes with damage could prove to be

advantageous for these materials. Several composite systems have been examined in the past, using the self-sensing principle of electrical resistance. Carbon fiber- reinforced polymer<sup>9-19</sup>, SiC fiber- reinforced polymer<sup>20-21</sup>, and carbon fiber- reinforced carbon<sup>15</sup> are a few examples of composites that show a change in electrical resistance upon mechanical loading and damage. For the case of fiber-reinforced polymer, conductive fibers are inside an insulating matrix. Electrical current is totally dependent upon the fiber properties and breaks. In a CMC system, such as the SiC/SiC composites studied here, the fibers and the matrix have similar conductivities. Therefore, both matrix cracking and fiber breaks will influence the electrical properties. Previous work with chemical vapor infiltrated (CVI) SiC/SiC composites has shown a direct relationship between matrix crack density and resistance change for samples subjected to creep conditions<sup>22</sup>. Room temperature monotonic tensile tests have also been conducted concerning this material<sup>23</sup>. Typically, the resistance changes were on the order of 50% for both test conditions. This study continued on the path of assessing damage in CMCs by studying the relationship between resistance change and matrix cracking for room temperature monotonic loading conditions of a melt infiltrated (MI) SiC/SiC composite.

Although the main focus of this paper was to study the electrical resistance change as a function of damage, a new acousto-ultrasonic (AU) scanning system was also employed for damage assessment and comparison. Ultrasonic methods that depend on plate waves provide a feasible option for assessing the health of CMC composites. These techniques are based on detecting changes in either the attenuation or speed of plate waves travelling through the material. Velocity variations correspond to stiffness (which, of course, is a dependent on the damage state) while attenuation measurements can be correlated to multiple types of damage (even in the absence of stiffness changes). Here, the focus was on studying the energy of the received ultrasonic pulse after it had traversed the material in the load direction. The new scanning device allows for planar images representing the relative attenuation of the ultrasonic pulses in a two dimensional region of interest.

## 2. PROCEDURE

### 2.1 Material

The composite samples used in this study consisted of Sylramic-iBN (Syl-iBN) fibers with a boron nitride interphase and a melt infiltrated (MI) matrix. The fibers were woven in a 2-D, five harness satin, with eight plies. Half the fibers were aligned with the load direction and half were perpendicular. Table 1 lists the specimen properties. All samples were cut from the same panel. The specimens were machined into 150 mm long tensile bars with a contoured gage section, as shown in Figure 1.

### 2.2. Test procedure and damage assessment

Tensile tests were performed using an Instron electro-mechanical, universal test machine. The grip regions of the samples were wrapped with copper mesh and gripped with rigidly mounted, hydraulically actuated wedge grips. A capacitance strain gage with a range of 1% over 25 mm was used to measure the extension of the gage section. Loading and unloading was performed at a rate of 4 kN per minute (~200 MPa/min). Unload-reload tensile hysteresis tests were performed at room temperature. Sample 1 was loaded until failure, with the load increasing by 1 kN (50 MPa) each loading cycle. Samples 2 and 3 were loaded directly to 5 and 6 kN (247 and 300 MPa), respectively, and then unloaded for further inspection (AU and sectioned for microscopy).

Electrical resistance was measured by a four-point probe method using an Agilent 34420A micro-ohmmeter. The copper mesh (Figure 1) was used not only to mechanically grip the samples (i.e., to increase friction in order to prevent slipping), but also functioned as an electrical contact. Furthermore, conductive silver paint was brushed on the specimen surface beneath the copper mesh to decrease contact resistance. Polymer tabs were adhered to the faces of the Instron metal wedge grips to electrically insulate the samples from the machine.

Modal acoustic emission (AE) was monitored throughout the test because it has been shown to correlate well with matrix cracking in MI CMCs<sup>24, 25</sup>. Piezoelectric sensors (50 kHz to 2.0 MHz) were placed near the grip area and clamped to the specimen surface. Vacuum grease was used as a couplant. The waveforms were recorded using a commercial eight-channel wave detector system produced by Digital Wave Corp. Software from the same company was used to filter the acoustic events in order to assure that only gage section events were analyzed.

The fundamental aspect of the AU method entails introducing a mechanical excitation at one point on a material surface and sensing the resulting disturbance at another spot on the material surface<sup>26</sup> with the aim of interrogating the material in between. A pulsing transducer is used to introduce a broadband, ultrasonic pulse into the specimen. The ultrasonic pulse is allowed to distribute itself diffusely into the specimen. For thin specimens, such as the ones examined here, multiple plate wave modes are excited. Various empirical parameters associated with the received signal are used to study the before-and-after behavior of the material of interest. AU parameters shown to correlate with distributed damage in SiC/SiC composites include the diffuse field decay rate, the mean square value (*MSV*) of the power spectrum, and the centroid of the power spectrum<sup>26, 27</sup>. An in-depth explanation of each of the terms is offered in Reference 26; this includes the associated equations and the detailed steps for obtaining the values. In summary, the diffuse field decay rate involves quantifying the internal damping of vibrational energy in materials. A greater decay rate indicates a greater amount of internal damping. The *MSV* of the power spectral density is defined as the area under the power spectrum curve of the received signal. Lastly, the centroid of the power spectrum represents the frequency demarcating the location of ultrasonic energy balance<sup>27</sup>.

Typically, the AU approach is implemented by monitoring a specimen's gage section behavior using two fixed transducers (i.e., in situ or interrupted). Recently, a scanning system was developed at the NASA Glenn Research Center that allows for the movement of the transducer pair, thereby, providing planar images representing localized AU behavior<sup>28</sup>. The system was used to conduct an area scan for two of the SiC/SiC specimens before and after tensile loading. The rectangular scan area was 8 mm x 100 mm (width x length) with x and y increments of 2 mm (50 steps) and 1mm (8 steps), respectively, as seen in Figure 1. The transducer contact force was controlled by an integrated load cell in order to assure consistent contact force throughout the scan. This is especially important for the *MSV* data where transducer pressures greatly influence the results.

Finally, a 25 mm section was cut from the gage region of each sample and polished to examine cracking. Since the matrix was in residual compression, the cracks had closed and become difficult to see. The polished samples were plasma etched with CF<sub>4</sub> gas at 600 Watts for 30 minutes. This process improves visibility of cracks in the CVI layer surrounding the fiber tows. Free Si in the MI matrix is also removed during this process, which makes it impossible to see the cracks in that region. Therefore, 'minimum crack density' values reported here reflect the cracks visible in the dense CVI layer. The interrupted samples likely had more cracks that were difficult to see even after etching, which is why the value reported here is deemed the minimum crack density.

### 3. RESULTS AND DISCUSSION

Figure 2 shows the applied stress and the resulting resistance change and the accumulated AE energy for each of the hysteresis loops. The resistance increased with rising stress and decreased as the load returned to zero. While unloading, the resistance decreased non-linearly until reaching a minimum 'residual' resistance at zero-load. The nonlinearity of the resistance during unload can be attributed to the closing of matrix cracks due to residual stresses in the matrix (note that the damage state remains constant during unload). While reloading, the resistance followed a similar non-linear trend until the previous maximum stress was exceeded. At that point, the resistance increased linearly (the AE events also resumed). Unlike the CVI material tested previously<sup>23</sup>, the cyclic loading resulted in a higher resistance for each cycle. That is to say, after unloading and then re-loading to the same stress, the resistance was higher than before. Since AE events were not detected during this portion of the re-loading, the resistance increase is not likely a result of crack growth. The exact reason for this behavior is unknown and requires further study, but may somehow be related to the closing and re-opening of cracks and de-bonding between the fibers and matrix in the crack region.

Just prior to failure, the total resistance change for Sample 1 was 504%, indicating very high sensitivity. It is also significant to note that for each of the specimens there was a permanent change in resistance that was observed even after unloading. The closing of the cracks caused a partial recovery regarding the matrix conductivity. Even so, the original electrical connections were never fully recovered. This phenomenon allows the technique to be utilized during component down times.

Stress-strain data is displayed in Figure 3 for all three samples. For clarity, the plots for Samples 2 and 3 are offset by 0.1%. Cumulative AE energy is also plotted (without offset) in Figure 3 for Sample 1. It should be noted that Sample 1 broke just outside the 25 mm extensometer, but still within the constant gage width. Samples 2 and 3 were loaded to 4

and 5 kN (i.e., 247 and 300 MPa), respectively, which corresponded to approximately 1/3 and 2/3 of the total AE energy, respectively. The correlation between AE and matrix cracking was studied in Reference 24. It was discovered that when AE energy was plotted versus stress, as in Figure 4, there was a short region of very low slope, followed by a sudden increase in slope. The low slope region was caused by the formation of micro-cracks. In MI composites, the micro-cracks initiated at the 90° surface bundles. These cracks did not penetrate the 0° tows until the stress increased to an ‘onset stress,’ which defined the point of increased slope for the accumulated AE energy. At that point, through-thickness and bridged cracks were seen. Fiber breaks mainly occurred at high stresses and were the major form of damage upon AE energy saturation. Based on this, through-thickness cracking was expected to form after the onset stress (i.e., 200 MPa). All samples in this study were interrupted beyond the onset stress and polished for crack examination. As a result, it was difficult to directly correlate the effect of these micro-cracks on resistance. However, Figure 2 shows that the resistance change of Sample 1 at 200 MPa was 5%. The resistance does change in response to these small micro-cracks, but was much more heavily dependent upon the through-thickness cracks and fiber breaks.

The microstructures of all three samples were examined for matrix cracks with an optical microscope. A photograph of the microstructure is shown in Figure 5. Since cracks in the MI matrix were undetectable due to the above described etching process, the minimum crack density was measured by counting the cracks in the thin layer of CVI surrounding the fiber tows. The results showed that the inner plies and surface plies had similar crack densities. The overall minimum crack densities are given in Table 1. As expected, Sample 1 had the highest crack density after being loaded to failure. Sample 2, which was loaded to approximately 1/3 of the AE energy, had approximately 1 crack for each visible 90° tow.

For MI systems, the AE energy has been shown to be directly proportional to crack density. Thus, AE energy was used in Figure 6 to predict the crack density as a function of stress, according to Reference 25. This was done by multiplying the normalized cumulative AE energy by the final crack density at failure. Figure 4 shows the prediction based on this calculation, compared with the measured minimum crack density of the three samples. Although based on a limited number of experimental data points, the data appears to show a linear relationship between crack density and applied stress. This differs slightly from the trend based on the AE data. As mentioned, the measured minimum crack density likely underestimates the actual crack density, which would explain the downward shift from the prediction.

To reiterate, the main objective of this study was to correlate matrix cracking with changes in electrical resistance. Figure 6 shows the relationship obtained for the three samples (i.e., resistance change versus crack density). The data fits a parabolic equation. It appears that the resistance was more sensitive to matrix cracks as the crack density increased. It is important to note, however, that there were additional damage mechanisms, such as fiber breaks, that occurred at the higher stresses. The number of fiber breaks is a difficult parameter to measure and is also less useful since the design community would frown upon excursions to such excessive loads.

Turning to the AU results, Figure 1 shows a typical AU image representing the mean square value of the power spectrum (gray scale in units of  $V^2$ ). Note that in addition to following the averages of each of the AU parameters for the entire 8 mm x 100 mm scan area, several subsets of the total area were assessed to study possible differences in AU behavior as a function of location. This included isolating the results for the central gage section as well as the transition areas near the specimen’s radii (see Figure 1 for overall scan area and subsets). For each of the parameters, it was found that the results were fairly consistent concerning the total scan area as well as the various subsets. This indicated a regular distribution of damage within the areas of interest. Table 2 summarizes the results, based on the total scan area, for the two specimens. As was the case in Reference 26, the most consistent results were based on the mean square value of the power spectrum. Here, large changes, greater than 70%, were observed after the damage inducing loads. In the earlier study, in situ monitoring during damage inducing tensile tests showed that large changes occurred early on due to both micro-cracking and transverse cracks. The values stayed fairly constant (i.e., a plateau) until near failure, at which point, fiber fractures caused further changes. The plateau was reached before transverse crack saturation and fairly early in respect to the AE accumulated energy plots. Since similar behavior was seen here, as witnessed by the indifference to the specific crack counts, it appears that these loads have reached the AU plateau. In summary, the scanning AU technique (especially the *MSV* term) was very sensitive to early matrix cracks, but to fully appreciate the capabilities of the new scan system, additional points of interruption are needed. This will be the focus of future studies which will also include interrupted creep tests.

## 4. CONCLUSIONS

Electrical resistance of MI SiC/SiC composites was monitored in situ during room temperature monotonic tensile tests for MI SiC/SiC composites. At the ultimate stress, the resistance had increased by over 500%. Permanent changes in resistance were also detectable after the load was removed (even with assumed crack closure). After polishing and examining the microstructure, a parabolic relationship between resistance and crack density was observed. This relationship can be used in future health monitoring efforts to estimate the crack density in situ. Acousto-ultrasonic scanning was also explored as a potential NDE technique for the composite. The AU scanning results were somewhat inconclusive because large changes were seen for both interrupted specimens with an indifference to the actual crack counts (using the mean square value of the power spectrum parameter). Based on the results here as well as past studies, this certain parameter appears to plateau fairly early during the transverse crack accumulation process (i.e., it's sensitive to micro-cracks and the early transverse cracks). Further changes are expected upon fiber fracture near failure (which is beyond the interruption points of these tests). Additional interruption points are needed in order to fully evaluate the potential of the system.

## ACKNOWLEDGEMENTS

The authors would like to thank the NASA Glenn Research Center at Lewis Field for providing funding for this study. This includes Dr. Joseph Grady and Dr. Anthony Calomino for support from the Hypersonics Project (Fundamental Aeronautics Program) and Dr. John Lekki and Dr. George Baaklini regarding the Vehicle Systems Safety Technologies Project (Aviation Safety Program).

## REFERENCES

- [1] Brewer, D., "HSR/EPM Combustor Materials Development Program," *Mater. Sci. Eng. A*, 261, 284–291 (1999).
- [2] Corman, G. S. et al., "Rig and Engine Testing of Melt Infiltrated Ceramic Composites for Combustor and Shroud Applications," *J. Eng. Gas Turbines Power.*, 124, 459–464 (2002).
- [3] Norris, G., "Weight Revolution- GE pushes for a breakthrough in lighter materials on back of JSF 136 engine," *Aviation Week and Space Tech.* 36, (2009).
- [4] Naslain, R. R., "SiC-Matrix Composites: Nonbrittle Ceramics for Thermo- Structural Application," *Int. J. Appl. Ceram. Technol.*, 2, 75–84 (2005).
- [5] Krenkel, W. and Berndt, F., "C/C–SiC Composites for Space Applications and Advanced Friction Systems," *Mater. Sci. Eng. A*, 412, 177–181 (2005).
- [6] Valentine, P. G., Rivers, H. K., and Chen, V. L., "X-37 C-SiC CMC Control Surface Components Development Status of the NASA Boeing USAF Orbital Vehicle and Related Efforts," Langley Research Center and Marshall Space Flight Center, (2003).
- [7] DiCarlo, J. A., Yun, H. M., Morscher, G. N., and Bhatt, R. T., [Handbook of Ceramic Composites], Springer, Berlin, 78–98 (2005).
- [8] Guillaumat, L., Lamon, J., "Multi-fissuration de Composites SiC/SiC," *Revue de Composites et des Materiaux Avances* 3, 159-171 (1993).
- [9] Wang, S., Chung, D. D. L., and Chung, J. H., "Impact damage of carbon fiber polymer–matrix composites, studied by electrical resistance measurement," *Composites A36*, 1707-1715 (2005).
- [10] Kupke, M., Schulte, K., and Schuler, R., "Non-destructive testing of FRP by d.c. and a.c. electrical methods," *Composites Sci. Technology* 61, 837-847 (2001).
- [11] Seo, D.-C. and Lee, J.-J., "Damage detection of CFRP laminates using electrical resistance measurement and neural network," *Composite Structures* 47, 525-530 (1999).
- [12] Abry, J. C., Choi, Y. K., Chateauminois, A., Dalloz, B., Giraud, G., and Salvia, M., "In-situ monitoring of damage in CFRP laminates by means of AC and DC measurements," *Comp. Sci. Technology* 61, 855-864 (2001).
- [13] Abry, J. C, Bochard, S., Chateauminois, A., Salvia, M., and Giraud, G., "In situ detection of damage in CFRP laminates by electrical resistance measurements," *Comp. Sci. Tech.* 59, 925-935 (1999).

- [14] Okuhara, Y. and Matsubara, H., "Memorizing maximum strain in carbon- fiber- reinforced plastic composites by measuring electrical resistance under pre- tensile stress," *Composites Sci. Tech.* 65, 2148-2155 (2005).
- [15] Chung, D. D. L., "Self-monitoring structural materials," *Materials Sci. and Eng.* R22, 57-58 (1998).
- [16] Todoroki, A., Omagari, K., Shimamura, Y. and Kobayashi, H., "Matrix crack detection of CFRP using electrical resistance change with integrated surface probes," *Comp. Sci. Tech.* 66, 1539-1545 (2006).
- [17] Wang, S. and Chung, D. D. L., "Self- sensing of flexural strain and damage in carbon fiber polymer-matrix composite by electrical resistance measurement," *Carbon* 44, 2739-2751 (2006).
- [18] Weber, I. and Schwartz, P., "Monitoring bending in carbon-fibre/ epoxy composite strands: a comparison between mechanical and resistance techniques," *Comp. Sci. Tech.* 61, 849-853 (2001).
- [19] Angelidis, N., Wei, C. Y. and Irving, P. E., "The electrical resistance response of continuous carbon fibre composite laminates to mechanical strain," *Composites A*, 35, 1135-1147 (2004).
- [20] Fankhanel, B., Muller, E., Fankhanel, T., and Siegel, W., "Conductive SiC-fibre reinforced composites as a model of smart composites," *J. Euro. Cer. Soc.* 18, 1821-1825 (1998).
- [21] Ogasawara, T., Aizawa, S., Ogawa, T. and Ishikawa, T., "Sensitive strain monitoring of SiC fiber/epoxy composite using electrical resistance changes," *Comp. Sci. Tech.* 67, 955-962 (2007).
- [22] Smith, C. E., Morscher, G.N., and Xia, Z.H., "Electrical resistance as a Nondestructive evaluation technique for SiC/SiC ceramic matrix composites under creep-rupture loading," *Int. J. Appl. Ceram. Technol.* 8, 298-307 (2011).
- [23] Smith, C. E., Morscher, G.N., and Xia, Z.H., "Monitoring damage accumulation in ceramic matrix composites using electrical resistivity," *Scripta Materialia* 59, 463-466 (2008).
- [24] Morscher, G.N., "Modal acoustic emission of damage accumulation in a woven SiC/SiC composite," *Comp. Sci. Tech.* 59, 687-697 (1999).
- [25] Morscher, G.N., "Stress- dependant matrix cracking in 2D woven SiC-fiber reinforced melt-infiltrated SiC matrix composites," *Comp. Sci. Tech.* 64, 1311-1319 (2004).
- [26] Gyekenyesi, A., Morscher, G., and Cosgriff, L., "In-Situ Monitoring of Damage in SiC/SiC Composites Using Acousto-Ultrasonics," *Composites Part B*, 37, (2006).
- [27] Roth, D., Verilli, M., Martin, R., Harmon, L., and Gyekenyesi, A., "High Frequency Ultrasonic Guided Wave Scan System for Characterization of C/SiC Composite Creep Damage," *Proc. Ceram. Eng. Sci.*, (2003).
- [28] Roth, D., Martin, R., Harmon, L., Gyekenyesi, A., and Kautz, H., "Development of a High Performance Acousto-Ultrasonic Scan System," *Proc. 29th Annual Review of Progress in Quantitative Nondestructive Evaluation*, (2002).

Table 1: Electrical resistivity and transverse crack density

Sample	Max Stress, MPa	Max Strain, %	Stiffness, GPa	First AE Stress, MPa	AE Onset Stress, MPa	Initial Resistivity, $\Omega$ -mm <sup>a</sup>	Resistance change, %	Minimum Etched Crack Density, mm <sup>-1</sup>
1	430	0.36	323	103	200	0.260	504	10
2	247	0.13	246	112	NA	0.267	17.9	0.9
3	300	0.21	237	119	200	0.251	78.5	3

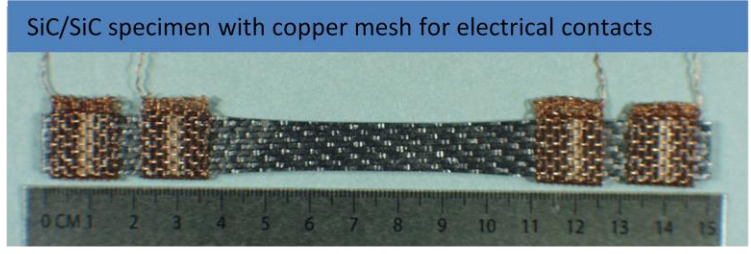
Note: all samples have eight plies with a BN interphase, 800 fibers per tow, and total fiber volume fraction of 0.38

<sup>a</sup> Resistivity estimated assuming constant gage width

Table 2: Acousto-ultrasonics results

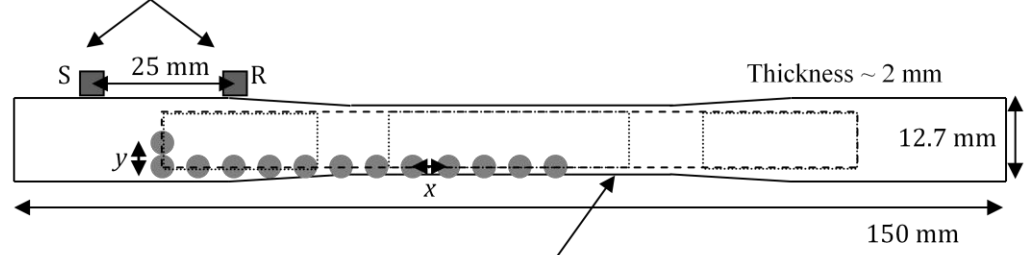
	Specimen 2			Specimen 3		
	Before test	After 247 MPa	Change, %	Before test	After 300 MPa	Change, %
Mean square value*, $V^2$	0.014 (0.007)	0.0031 (0.0014)	-77	0.015 (0.008)	0.0046 (0.0022)	-70
Centroid*, MHz	0.349 (0.010)	0.350 (0.015)	0.3	0.35 (0.01)	0.354 (0.014)	1.1
Diffuse field decay rate*, $V^2/\mu\text{sec}$	0.011 (0.005)	0.015 (0.005)	36	0.011 (0.006)	0.012 (0.004)	9.0

\* Data represents the average for the overall scan area (standard deviations indicated within parenthesis).



a

Transducers (1.25 MHz, broadband)



b

Main AU scan area (dashed line, with sub-areas defined by dotted lines) and result screen below.

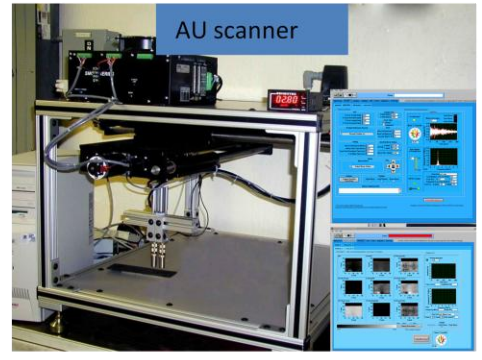
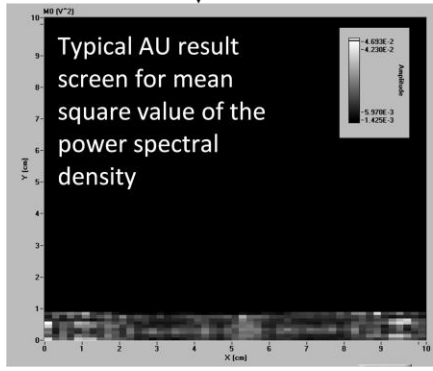


Figure 1: a) Photo of specimen with copper mesh for mechanical gripping and electrical contact b) AU set-up for inspecting damage.

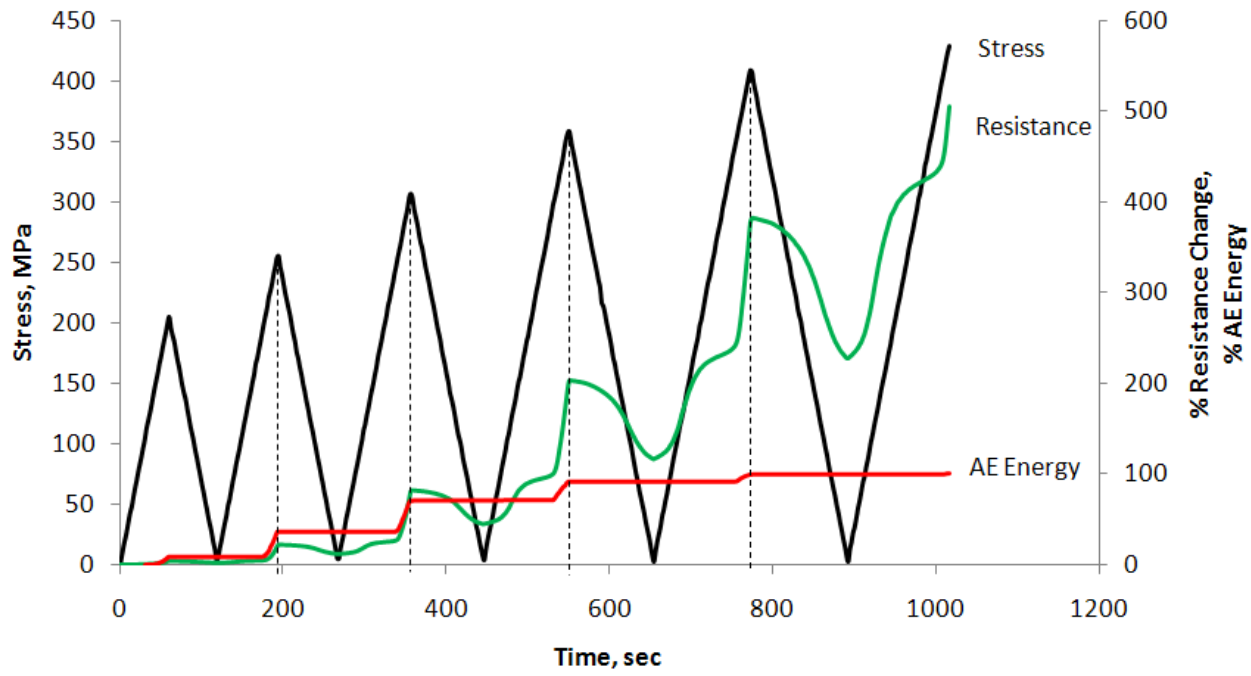


Figure 2: Applied stress, resistance change, and AE energy released

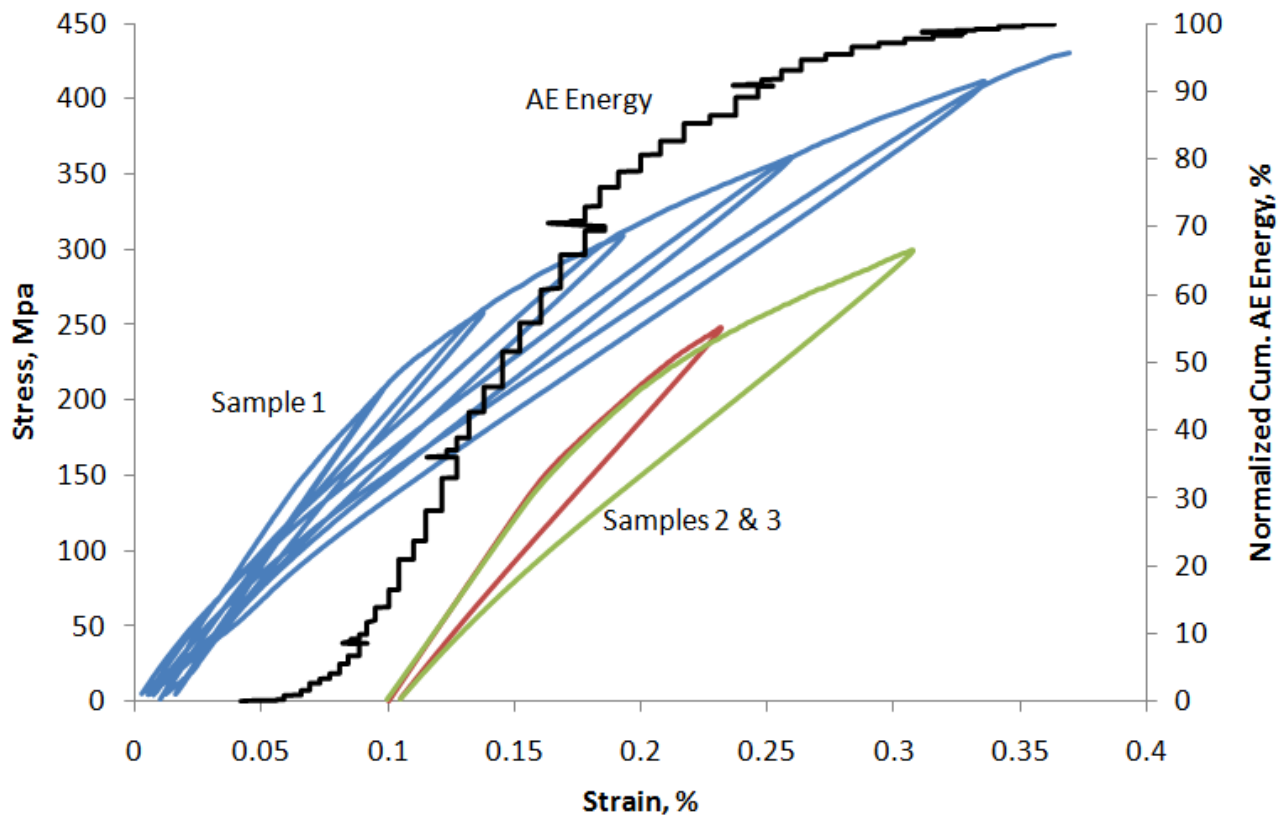


Figure 3: Stress-strain for all three samples and AE energy for sample 1. Note: Plots for samples 2 and 3 are offset by 0.1% for clarity.

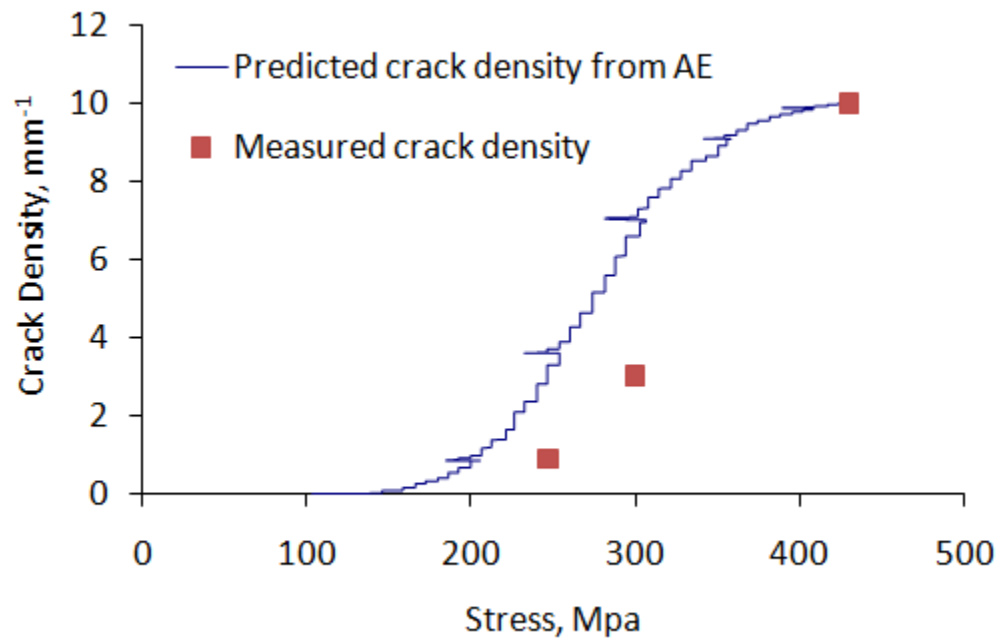


Figure 4: Measured crack density for samples 1-3, along with predicted crack density based on AE energy



Figure 5: Microstructure after etching

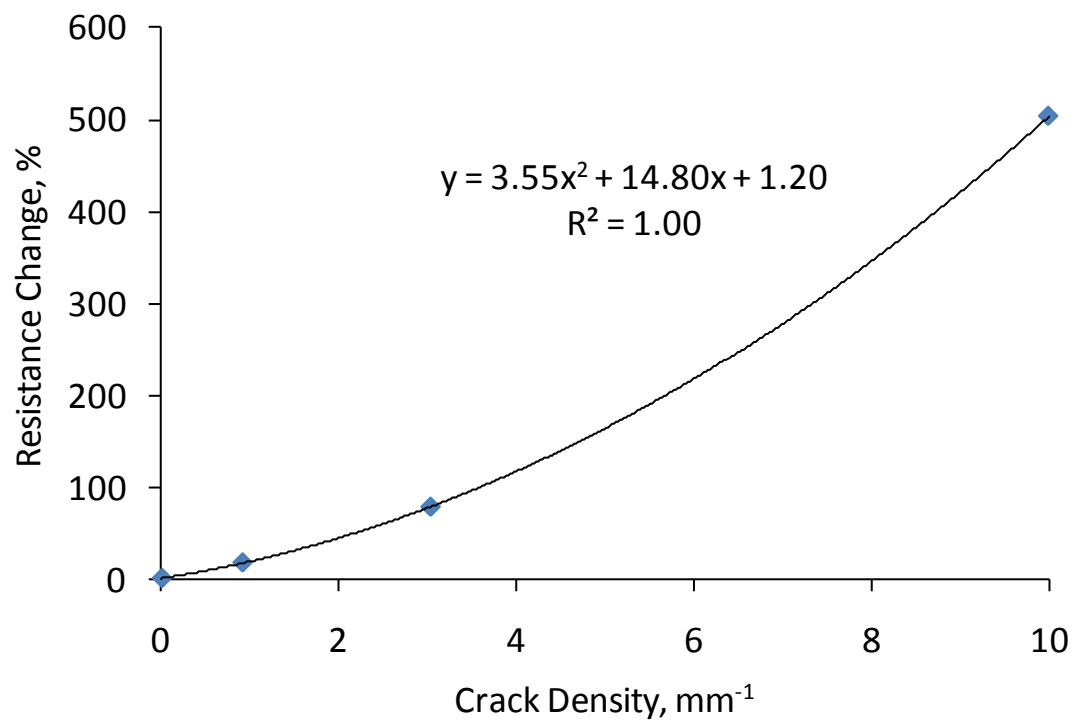


Figure 6: Maximum resistance change versus measured crack density for all samples